

Optical, Photoelectrochemical, and Electrochemical Impedance Studies on Photoactive Organic/Inorganic/Interface Assemblies of Poly 2,2 Bithiophene/Poly 3-(2-Thienyl) Aniline (PThA)/TiO₂

Kasem K. Kasem^{1*}, Houria Sadou², Henry Worley¹, Jordan Wenger¹

¹School of Sciences, Indiana University Kokomo, Kokomo, IN, USA

²Laboratoire de Chimie des Matériaux Inorganiques et Applications, University of Sciences and Technology of Oran-Mohamed Boudiaf, Oran, Algeria

Email: *kkasem@iuk.edu

How to cite this paper: Kasem, K.K., Sadou, H., Worley, H. and Wegner, J. (2018) Optical, Photoelectrochemical, and Electrochemical Impedance Studies on Photoactive Organic/Inorganic/Interface Assemblies of Poly 2,2 Bithiophene/Poly 3-(2-Thienyl) Aniline (PThA)/TiO₂. *Journal of Materials Science and Chemical Engineering*, 6, 50-67.
<https://doi.org/10.4236/msce.2018.68005>

Received: July 11, 2018

Accepted: August 28, 2018

Published: August 31, 2018

Copyright © 2018 by authors and Scientific Research Publishing Inc.

This work is licensed under the Creative Commons Attribution International License (CC BY 4.0).

<http://creativecommons.org/licenses/by/4.0/>



Open Access

Abstract

Particles of TiO₂ modified with poly 3-(2-thienyl) aniline (PThA) and occluded in poly 2,2 bithiophene (PBTh), were subjected to optical, electrochemical impedance spectroscopic (EIS) and photoelectrochemical (PEC) investigation in aqueous, acetate, citrate, and phosphate electrolytes. EIS studies revealed that the assembly film of TiO₂/PThA/PBTh possess porous-type structure. They also confirmed the approximate value of E_f obtained from electrochemical studies. Both EIS and optical studies indicated that ac conductivity is much greater than dc conductivity. Guided by the properties of PBTh, no large changes in the energy band structure occurred due to occlusion of TiO₂ in PBTh films. Occlusion of TiO₂/PThA into the network structure of PBTh inhibits the energy dissipation process and impeded charge polarization process of the material. Photoelectrochemical outcome suggested possible band alignments between the organic film and TiO₂ and formation of hybrid sub-bands. Inclusion of TiO₂ in the thiophene-based polymers enhanced the charge separation and consequently charge transfer processes and widen the absorption in visible light range.

Keywords

TiO₂, Organic Polymers, Photoactive Interfaces, Optical, Organic Semiconductors and Impedance Spectroscopy

1. Introduction

An important method for creation or elimination of defects in solid materials is surface or bulk modification of inorganic/organic interfaces. This method will also alter the donor/acceptor character of these interfaces. The charge production, separation, and transfer at these interfaces were the subject of several investigations. Hybrid interfaces, such as those at the hetero-junction of inorganic/organic interfaces (IOI) recently became the focus of several research efforts [1]-[6].

Because of its chemical stability, TiO_2 was subjected to many investigations compared to other photoactive metal oxides. TiO_2 -based heterojunction assemblies were included in several applications [7]-[20]. Enhancing the photoelectrical performance of a dye-sensitized solar cell was achieved by doping SrTiO_3 : $\text{Sm}^{3+}/\text{SiO}_2$ core-shell nanoparticles in the cell's photoanode [7] [17]. Several applications used TiO_2 -based interfaces for water splitting and hydrogen production [8] [15], photocatalysis [9] [13], and solar cells [12]. Involving TiO_2 in photoactive self-cleaning polymer coatings was also recently reported [14] [20].

Occlusion electrodeposition (OE) is one of the most effective methods for building photoactive assemblies of hybrid thin film interfaces. OE has been used to build composite films containing occluded TiO_2 [21] [22] [23] [24] or CdS [25] [26] particles within other matrices.

In this article, we investigated difference(s) in optical, electrical properties, and photoelectrochemical behaviors caused by the occlusion of TiO_2 surface modified with PThA in organic polymers Poly Bithiophene (PBTh). In particular, we studied the changes in the photocurrent generation as an indicator for this assembly's ability to cause the photoinduced charge separation. Further electrochemical impedance spectroscopy (EIS) studies were used to investigate changes in electrical properties, such as dielectric constants and electrical conductivity. The host matrix was produced by electro-polymerization of 2,2 bithiophene (BTh) which forms polymeric networks suitable for efficient occlusion. The optical parameters such as the optical conductivity (σ_{opt}), optical absorption coefficient (α), refractive index (n), real dielectric constants (ϵ_r), and imaginary dielectric constants (ϵ_i) were also investigated.

2. Experimental

2.1. Reagents

The monomers 2,2 bithiophene (BTh), and 3-(2-thienyl) aniline (ThA) (Alfa Aesar) were used to prepare their corresponding polymers; poly 2,2 bithiophene (PBTh) and poly 3-(2-thienyl) aniline (PThA), respectively. All of the chemicals used were of analytical grade and used as received from the vendors. Unless otherwise stated all of the solutions were prepared using deionized (DI) water.

2.2. Preparations

Surface modified TiO_2 nanoparticles were prepared as previously described [27],

briefly; suspensions of TiO₂/P2ThA interface were prepared as follows: 0.05 g of TiO₂ nanoparticles were suspended in the solution of 2ThA in acetonitrile. The mixture was subjected to a 10 minute sonication followed by stirring for 1.0 hour to allow maximum adsorption of 2ThA on the TiO₂ nanoparticles. The excess 2ThA was removed by centrifugation. The IOI thin films were prepared using occlusion method; thin films of TiO₂ modified with PTHA/PBTh were generated electrochemically using cyclic voltammetry (CV) by repetitive cycling of the FTO electrode potential between -0.5 and 1.7 V vs Ag/AgCl in an acetonitrile suspension (1 mg/mL) of TiO₂, 1 mM of the BTh monomer, and 0.5 M LiClO₄.

2.3. Instrumentation

A conventional three-electrode cell consisting of a Pt wire as a counter electrode, a Ag/AgCl reference electrode, and FTO with surface area 2.0 cm² as working electrode was used for electrochemical studies. Photoelectrochemical studies on the thin solid films were performed on the experimental setup as described in previous work [27]. A Solartron 2101A was used for EIS studies. A BAS 100W electrochemical analyzer (Bioanalytical Co.) was used to perform the electrochemical studies. Optical parameters were calculated based on the steady state reflectance spectra, measured by a Shimadzu UV-2101PC spectrophotometer. An Olympus BX-FL reflected light fluorescence microscope, working with polarized light at wavelengths ranging between 330 and 550 nm was used to visualize the surface imaging of the film. Irradiation was performed with a solar simulator 300-watt xenon lamp (Newport, NJ) with an IR filter. All measurements were performed at 298 K.

3. Results and Discussion

3.1. Optical Studies

Optical parameters such as σ_{opt} , α , skin factor, n , ϵ_r and ϵ_i have been calculated and plotted as a function of photon energy. The results are displayed in **Figures 1-5**.

3.1.1. Optical Band Gap Studies

The absorption spectra of the TiO₂/PThA/PBTh assembly displayed in **Figure 1(A)** indicates that occlusion of TiO₂ shifts the absorption peak to higher photon energies than that of the host polymer PBTh. **Figure 1(B)** and **Figure 1(C)** were prepared after treatment of the absorption data as plots of $\alpha^{1/2}$ vs photon energy ($h\nu$) and $(\alpha^* h\nu)^2$ vs $h\nu$, respectively, as described in previous study [28]. The value of α was calculated using a film thickness of 1.0 μm . **Figure 1(B)** and **Figure 1(C)** indicated that the absorption behavior of the host film was dominating the assembly behavior. Both the host polymer, PBTh, and the assembly showed direct and indirect band gaps. This is because the occlusion of TiO₂, modified with PThA, created hybrid sub-bands with smaller band gaps between the highest occupied molecular orbitals (HOMO) and lowest unoccupied molecular

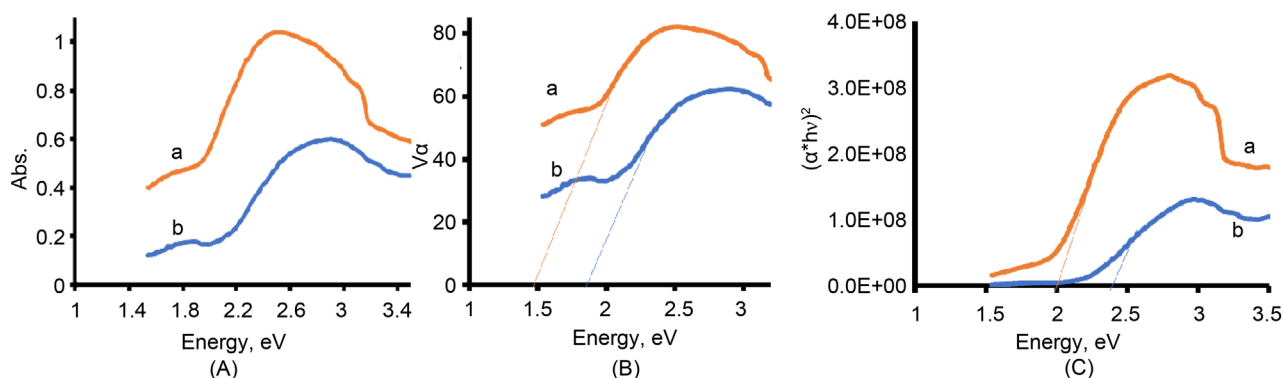


Figure 1. (A) Absorption spectra (B) $\alpha^{1/2}$ ($\text{cm}^{-1/2}$) vs photon energy (C) $(\alpha \cdot hv)^2$, $(\text{eV} \cdot \text{cm})^2$ vs photon energy for (a) PBTh and (b) $\text{TiO}_2/\text{PThA}/\text{PBTh}$.

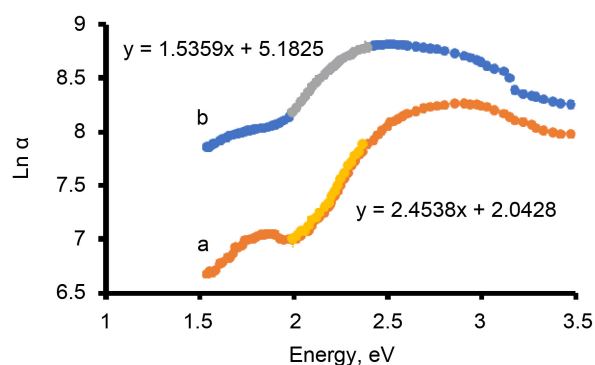


Figure 2. Plot of $\text{Ln } \alpha$ vs photon energy for (a) PBTh and (b) $\text{TiO}_2/\text{PThA}/\text{PBTh}$.

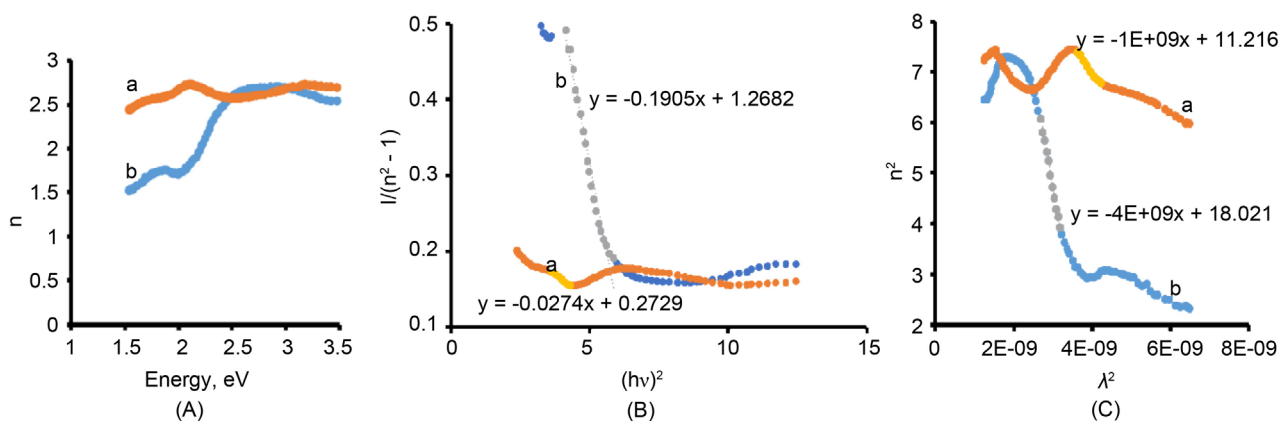


Figure 3. (A) Refractive index n vs photon energy, (B) $1/(n^2 - 1)$ vs $(hv)^2$, and (C) n^2 vs λ^2 for (a) PBTh and (b) $\text{TiO}_2/\text{PThA}/\text{PBTh}$.

orbitals (LUMO) of the host polymer. Results shown in **Figure 1** also indicate existence of absorption band tails attributed to energy band tail, also known as Urbach energy [29].

Figure 2 shows the plot of $\text{Ln } \alpha$ vs photon energy for the host polymer and for the assembly. The rising linear portion of the plot (indicated by colors) exhibits slopes of 1.536 and 2.454 for the assembly and the host respectively. These values

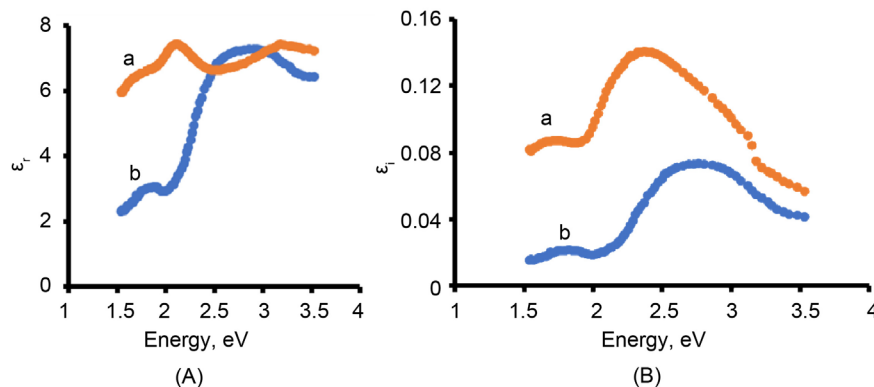


Figure 4. (A) Real ϵ_r , and (B) imaginary ϵ_i components of dielectric constant for (a) PBTh and (b) TiO₂/PThA/PBTh.

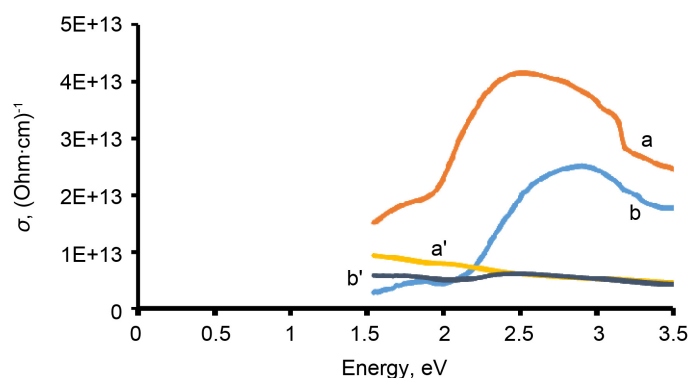


Figure 5. Conductivity (optical σ_{opt} & electrical σ_{ele}) vs photon energy, (a) σ_{opt} and, (a') σ_{ele} for PBTh, and (b) σ_{opt} and (b') σ_{ele} for TiO₂/PThA/PBTh.

correspond to Urbach energy (energy band tail) values of 0.651 eV and 0.407 eV for the assembly and for the host PBTh, respectively. These value of energy band tail reflects the amorphous nature of the material; the greater the energy band tail, the greater the amorphous nature of the material. This indicates that occlusion of TiO₂ modified particles into PBTh increased the degree of amorphousness of the assembly.

3.1.2. Optical Parameters

1) Refractive index, n

Figure 3(A) displays the plot of refractive index (n) vs photon energy. Although both materials exhibit a large increase in n when the photon's energy is greater than 2.0 eV, the value of n for TiO₂/PThA/PBTh is smaller than that of PBTh up to ≈ 2.5 eV, after which both n values are approximately equivalent. **Figure 3(A)** shows that both PBTh and TiO₂/PThA/PBTh exhibits a normal dispersion region up to 2 eV or at λ 620 nm. At this region, both systems obey a single oscillator model. At λ shorter than 620 nm, an anomalous dispersion (multi-oscillator model) can be applied.

At region of normal dispersion, the following equation can be applied [30]:

$$\left[n^2 (hv) - 1 \right]^{-1} = \frac{-1}{E_o E_d} (hv)^2 + \frac{E_o}{E_d} \quad (1)$$

where E_o is oscillator energy, and E_d is the dispersion energy. Plotting the values of $1/(n^2 - 1)$ vs $(hv)^2$ in the region of single oscillator model, the values of E_o and E_d can be obtained from the slope and the intercept of the obtained line. **Figure 3(B)** displays the plots for both PBTh and TiO₂/PThA/PBTh. The calculated E_o and E_d values for PBTh are 3.179 and 11.65 eV, respectively, while E_o and E_d for TiO₂/PThA/PBTh are 2.58 and 2.035 eV respectively. As E_d is a measure of the inter band intensity, it can be concluded that occlusion of TiO₂/PThA into PBTh reduced this intensity evident from the lower E_d of TiO₂/PThA/PBTh than that of PBTh.

Figure 3(C) was created following the relation [31]:

$$n^2 = \varepsilon_L - \left[\frac{e^2}{\pi C^2} \right] \left[\frac{N}{m^*} \right] \lambda^2 \quad (2)$$

The intercepts of the linear equations displayed in the **Figure 3(C)** denote to ε_L lattice dielectric constant. These intercepts are 11.216 and 18.021 for PBTh and for TiO₂/PThA/PBTh, respectively. This indicates that occlusion of TiO₂/PThA into PBTh increased the lattice dielectric constant.

2) Dielectric constants, real ε_r , and imaginary ε_i

Figure 4 displays the plots of the calculated ε_r and ε_i against photon energy. The plot of the ε_r vs photon energy is displayed in **Figure 4(A)**. This figure shows a pattern similar to that displayed in **Figure 3(A)**. As ε_r was calculated from the relation $\varepsilon_r = n^2 - k^2$, and as $n \gg k$, we can approximate that ε_r is directly proportional to n . On the other hand, **Figure 3(B)** shows the change in ε_i vs photon energy. It can be noticed that ε_i for the host polymer is greater than that of the hybrid assembly. The ε_i started increasing around the absorption edge and reach its maximum value when photon energy reached ≈ 2.5 eV for PBTh, and about 2.8 eV for TiO₂/PThA/PBTh.

The results displayed in **Figure 4(A)** show that the ε_r of PBTh and that of TiO₂/PThA/PBTh assembly have closer values around a photon energy range between 2.2 to 3.0 eV. Above and below this range the real dielectric part for TiO₂/PThA/PBTh was less than that of PBTh. As the real part of the dielectric is related to polarization and anomalous dispersion, the ε_r indicates how much occlusion of TiO₂/PThA/PBTh enhanced the speed of light in the material [32].

The results displayed in **Figure 4(B)** show that: the ε_i of TiO₂/PThA/PBTh assembly is less than that calculated for the host polymer PBTh. Such behavior can be explained considering that the TiO₂/PThA nanoparticles occluded into PBTh inhibit the energy dissipation process [33]. Because ε_i is associated with dissipation of energy into the medium, the ε_i signifies the influence of dipole motion on energy absorption by the dielectric material from an electric field.

3) Optical conductivity σ_{opt} and Electrical conductivity σ_{ele}

Both σ_{opt} and σ_{ele} were calculated using the following formulas [34] [35] [36]:

$$\sigma_{opt} = \frac{\alpha nc}{4\pi} \quad (3)$$

and

$$\sigma_{ele} = \frac{2\lambda\sigma_{opt}}{\alpha} \quad (4)$$

The plots of σ_{opt} and σ_{ele} vs photon energy for PBTh and for TiO₂/PThA/PBTh is displayed in **Figure 5**.

Figure 5 clearly shows that 1) σ_{opt} for PBTh is greater than that of TiO₂/PThA/PBTh, 2) σ_{opt} increases with increasing photon energy up to 2.5 eV for PBTh, and up to 3.0 eV for CdS/PThA/PBTh. The lower optical conductivity of TiO₂/PThA/PBTh than PBTh is due to the presence of modified TiO₂/PThA nanoparticles as a dopant in PBTh network structure. **Figure 5(B)** indicates that the dopant lacks the ability to provide the host polymer with an additional charge transfer [34]. Incident light interacts with charges of the material as a result of absorption of photon energy by the assembly. The presence of TiO₂/PThA impeded the charge polarization process of the material. This means that the TiO₂/PThA/PBTh negatively affected the dissipation of energy into the host PBTh film. This is consistent with the results displayed for the ϵ_i vs photon energy displayed in **Figure 4(B)**. **Figure 5(a')** and **Figure 5(b')**, also shows that σ_{ele} for each of PBTh, and for TiO₂/PThA/PBTh are smaller than the corresponding σ_{opt} . However, they increase slightly with decreasing the photo energy. Such behavior can be explained on the bases of the Drude model [37]. As electrical conductivity is considered as optical conductivity in a lack of alternating field (frequency), at lower photon energy optical conductivity will be under lower frequency.

3.2. Photoelectrochemical Behavior

The previous investigation done on the host polymer PBTh [27] was used to compare and draw conclusion on the contribution of the occluded TiO₂/PThA to the photo activity outcome of the TiO₂/PThA/PBTh assembly. Unless otherwise noted, the photoelectrochemical behavior was investigated in the dark and under illumination by cycling the potential of FTO/TiO₂/PThA/PBTh between -1.0 to 1.0 V vs. Ag/AgCl at a scan rate of 0.10 V/s in a given electrolyte. The electrode surface area was kept at 2.0 cm².

3.2.1. Electrochemical Behavior of the TiO₂/PThA/PBTh Assembly in Aqueous Acetate Electrolyte

The behavior of the FTO/TiO₂/PThA/PBTh assemblies was investigated in 0.2 M acetate electrolyte (pH 8). **Figure 6(A)** shows that the recorded photocurrent is greater than the current recorded in the dark in the cathodic scan at ≈ 0.30 vs Ag/AgCl. This means that the approximate E_{fb} (flat band potential) of the assembly is at ≈ 0.30 V or 0.50 V vs SHE. (**Table 1**). The photocurrent-time

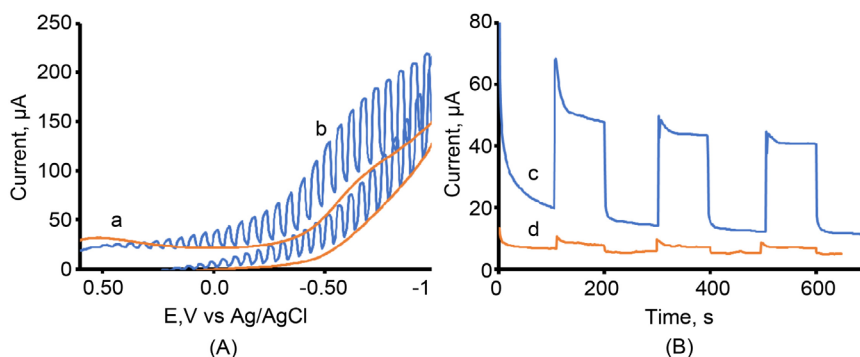


Figure 6. Photoelectrochemical behavior of TiO₂/PThA/PBTh in 0.2 M acetate electrolyte (A) CV at 0.1 V/s, in (a) dark (b) illumination; (B) Photocurrent vs time curve at -0.5 V vs Ag/AgCl (c) in the presence of O₂, (d) after purge with N₂.

Table 1. Photoelectrochemical data for the TiO₂/PThA/PBTh.

Property	PBTh	TiO ₂ /PThA/PThA	PThA	TiO ₂
IP, EV	5.6	5.6	5.28	7.40
E_g , eV	2.55	2.80	2.40	3.10
EA	3.05	2.8	≈2.90	4.30
E_g , eV	5.40	≈5.4	5.00	Doping Depend

IP = ionization potential, E_g = band gap, EA = electron affinity.

curve displayed in **Figure 6(B-c)**, **Figure 6(B-d)** was generated by subjecting the FTO/CdS/PThA/PBTh assembly to illumination at constant potential (-0.5 V vs Ag/AgCl). Upon illumination of an oxygenated electrolyte, a sharp current spike shown in the first trail followed by steady small changes for longer time **Figure 6(B-c)**. This behavior was reproducible but with a smaller magnitude in the following trials. Such behavior is indication of fast charge recombination due to hole accumulations at the outermost layers of the assembly/electrolyte interface [38]. When the experiment was repeated in deoxygenated electrolyte (using N₂ gas), the illumination generated much less photocurrent (**Figure 6(B-d)**). **Figure 6(B)** also shows a reduction in the capacitive current in the deoxygenated electrolyte compare to that in presence of oxygen. These results assume that O₂ plays an important role in enhancing charge separation during the illumination period.

3.2.2. Electrochemical Behavior of the TiO₂/PThA/PBTh Assembly in Aqueous Citrate Electrolytes

Figure 7 displays the electrochemical behavior of FTO/TiO₂/PThA/PBTh in aqueous citrate electrolyte (pH 8). This figure shows that at ≈0.5 V vs Ag/AgCl, the photocurrent exceeds the current recorded in the dark for citrate electrolyte (**Figure 7(A)**) in the cathodic scan, we assume that the value of the hybrid sub-band is at ≈0.7 V vs SHE.

The photocurrent vs time curve in **Figure 7(B)** shows a behavior comparable to that observed in **Figure 6(B)** (acetate electrolyte). However, upon illumination

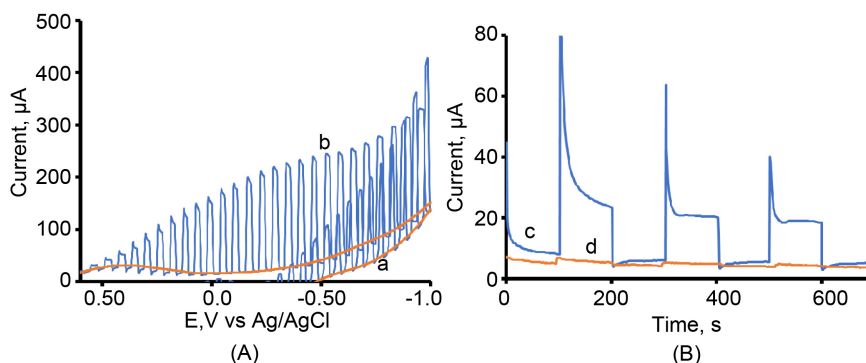


Figure 7. Photoelectrochemical behavior of FTO/TiO₂/PThA/PBTh in 0.2 M Citrate electrolyte (pH 8) (A) CV at 0.1 V/s a) dark, (b) illumination; (B) Photocurrent vs time curve at -0.5 V vs Ag/AgCl (c) in the presence of O₂, and (d) after purge with N₂.

of the oxygenated citrate electrolyte (**Figure 7(B)**), a reproducible larger sharp anodic current spike is observed. Such phenomena were more noticeable in the deoxygenated electrolyte (**Figure 7(B-b)**). When the light is off there is evidence for reversed transient current, as evident by the small cathodic current spike at the first few seconds in dark. This is due to backflow of electrons from the substrate FTO to the assembly body.

When the electrolyte was deoxygenated, illumination generated much less photocurrent. This behavior was reproducible through multiple cycles of illumination and darkness. The photocurrent generated in citrate is greater than that generated in acetate.

3.2.3. Electrochemical Behavior of the TiO₂/PThA/PBTh Assembly in Aqueous Phosphate Electrolyte

Figure 8 displays the electrochemical behavior of TiO₂/PThA/PBTh in 0.2 M phosphate electrolyte (pH 6) in dark and under illumination. **Figure 8(A)** shows that at ≈ 0.4 V vs Ag/AgCl (0.6 V vs SHE), the recorded photocurrent exceeds that measured in the dark during the cathodic scan. The manual chopping of light experiment indicates that the assembly is highly responsive to the illumination-dark cycles. Furthermore, **Figure 8(B)** shows the photocurrent-time curve under a constant potential (ca -0.500 V vs Ag/AgCl) with illumination for a longer period of time. Upon illumination in the oxygenated phosphate electrolyte (**Figure 8(B-c)**), a sharp anodic current spike, similar to that observed in the citrate was obtained. In darkness, there is no evidence for reversed transient current. This means that no backflow of electrons from the substrate FTO to the assembly body took place. When the electrolyte was deoxygenated using nitrogen gas (**Figure 8(B-d)**), much less photocurrent was recorded with behavior similar to that observed in the oxygenated solution.

Upon illumination of the oxygenated phosphate electrolyte (**Figure 8(B-a)**), a sudden increase in the photocurrent was recorded followed by a steady decrease in photocurrent to constant quantity. The initial decay reflects some e/h recombination. The photocurrent vs time curve for the host polymer PBTh only [27] is

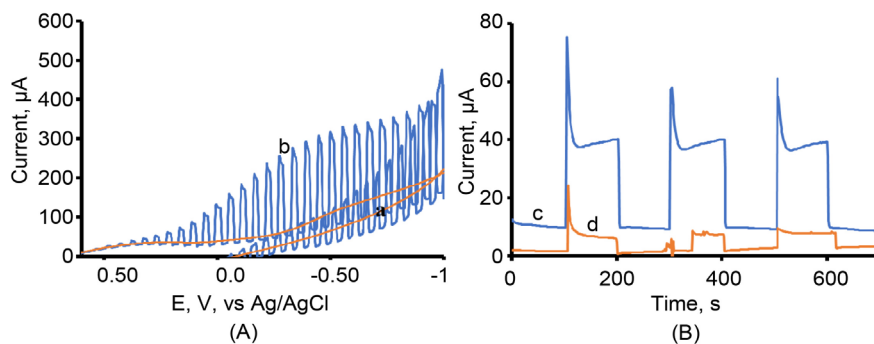


Figure 8. Photoelectrochemical behavior of $\text{TiO}_2/\text{PThA}/\text{PBTh}$ in 0.2 M phosphate electrolyte (pH 6). (A) CV at 0.1 V/s (a) dark, (b) illumination; (B) Photocurrent vs time curve at -0.5 V vs Ag/AgCl (c) in the presence of O_2 , and (d) after purge with N_2 .

smaller than that observed in **Figure 8(B)**. This indicates that occlusion of TiO_2 enhanced the photocurrent generation as a result of improvement of the photo-induced charge separation.

We further investigated the effect of changing the pH on the E_{fb} of this assembly. No changes in E_{fb} were observed within the pH 5 - 8 range. A change of approximate 2 pH units did not affect the position of E_{fb} in the sulfur-based assembly. The relation between E_{fb} and pH in oxide-based semiconductors, changes by 25 mV per change in 1 pH unit.

Oxygen involvement in the photochemical activities is in the electron consumption processes illustrated by the equation:



As PBTh act as p-type semiconductor where holes are the charge carrier. When the outermost layer of the assembly is hit by suitable photon energy, this creates a shorter diffusion course to photogenerated holes to reach the adsorbed anions on the surface of the assembly. This makes the hole consumption by the used electrolytes anions is important step in the mechanism of charge separation.

The following explains the oxidation of the studied anions at the electrolyte $\text{TiO}_2/\text{PThA}/\text{PBTh}/\text{electrolyte}$ interface.

For oxidation of phosphate anion, a formation of phosphate radical anion [39] can prevent the e/h recombination process according to Equation (6),



Involvement of both oxygen and phosphate in the charge separation process that lowers the e/h recombination is explained by Equations (5) and (6).

In case of carboxylic anions, a Kolb-type reaction [40] causes photooxidation of carboxylate anions according to the following equation:



3.2.4. Electrochemical Impedance Spectroscopic Studies

Impedance spectra of the $\text{FTO}/\text{TiO}_2/\text{PThA}/$ or FTO/PBTh was measured and

analyzed on three-electrode cell containing liquid electrolytes, between $10^5 - 10^{-2}$ Hz utilizing Solartron 1201A, MX-studio ECS software. Impedance complexes (Nyquist plot) generated from these studies are displayed in **Figure 9**. This Figure shows both kinetic control at high frequency and diffusional control at low frequency. The shape of unconcentrated semicircle in at high frequencies and existence of Warburg impedance reflects the film porosity [41]. The calculated C_{dl} was 7.43×10^{-5} F. The maxima of the semicircle corresponded to relaxation frequency of 1.25Hz, which is 0.79 s relaxation time.

Using equivalent circuit and modeling approach by Randel [42], the reaction rate at the assembly interface can be calculated. The difference between R_{ct} and the intercepts of the tangent line of Warburg diffusional region equals to $[(R_{ct} \times \lambda)^2 \times C_{dl}]$, where $\lambda = \frac{k}{\sqrt{D}}$, k is rate constant, and D is the diffusion coefficient.

Knowing (λ) and D , k can be calculated For Warburg frequency region (the very low frequencies), plotting the Z'' vs $1/\omega$ (**Figure 9** inset) generates a straight line with $\text{slop} = 1/C_L = 191 \text{ F}^{-1}$. Substituting the approximate R_L value of 5000 ohm, the diffusion coefficient can be determined using the following equation:

$$R_L = \frac{1}{C_L} * \frac{L^2}{3D_{CT}} \quad (8)$$

For $L = 1 \mu\text{m}$, the calculated D was $= 5.65 \times 10^{-10} \text{ cm}^2/\text{s}$. The calculated k under dark condition is $1.89 \times 10^{-5} \text{ cm/s}$, while under illumination k is $2.22 \times 10^{-5} \text{ cm/s}$.

1) Dielectric constants

Figure 10 Shows that dielectric constants increased at very low frequencies. As frequency increased, the values of the dielectric constants decreased. Such

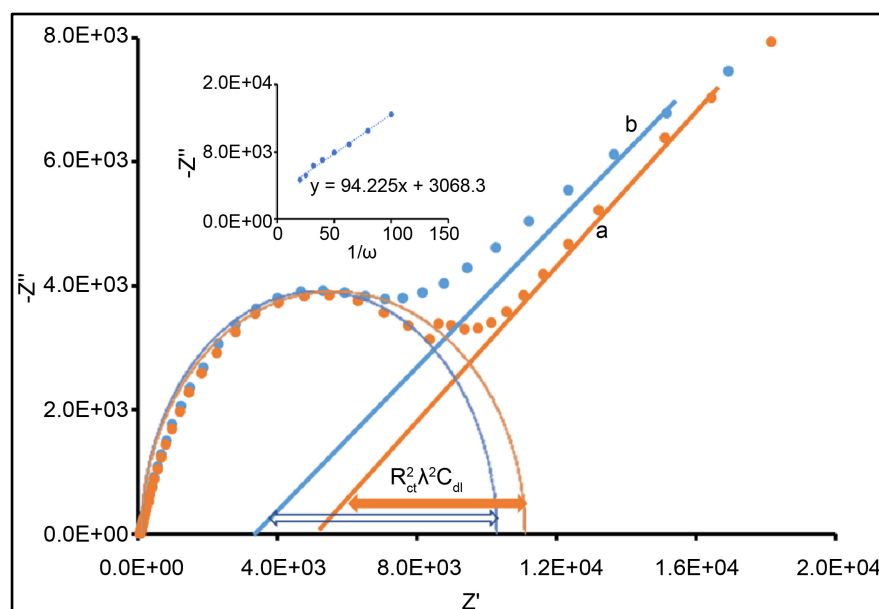


Figure 9. Nyquist plot of $3 \mu\text{m}$, $\text{TiO}_2/\text{PThA}/\text{PBTh}$ film on FTO in 0.2 M acetate electrolytes (pH 6) at 0.5 V vs Ag/AgCl (a) dark, (b) light.

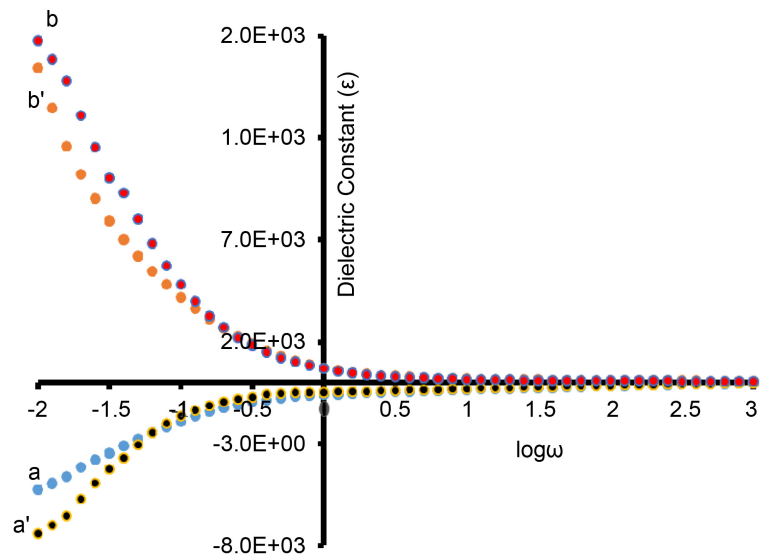


Figure 10. Plot of dielectric constant ϵ vs $\log \omega$ (a) real dielectric component (ϵ_r), and (b) imaginary component (ϵ_i) under illumination, (a') ϵ_r and (b') ϵ_i in dark, in acetate electrolyte (pH 8).

behavior was previously observed and attributed to the inability of the electric dipoles to comply with variation of an applied a.c. electric field [43]. Materials that possess conducting grains, but with poor conducting borders causes charge carriers accumulated at these borders, when external external electric field (low frequency) is applied. This creates large polarization and consequently a high dielectric constant [44].

2) AC conductivity σ_{ac}

The σ_{ac} was calculated using the following equation [45].

$$\sigma_{ac} = \frac{L}{A} * \frac{Z'}{Z'^2 + Z''^2} \quad (9)$$

According to the following equation [46]:

$$\sigma_{ac} = \sigma_{dc} + A\omega^s \quad (10)$$

where A is the strength of polarizability, s is temperature dependent parameter which can be determined from the slope of line of the plot of $\log \sigma_{ac}$ vs $\log \omega$.

$$\log \sigma_{ac} = \log \sigma_{dc} + \log A + S \log \omega \quad (11)$$

Figure 11 was constructed to show the plot of calculated $\log \sigma_{ac}$ vs $\log \omega$ at different frequencies. This figure clearly shows the positive correlation between σ_{ac} and ω at the high dispersive region of high frequencies range up to several kHz. The slope of the line (s) was = 0.7901, which indicates the hopping due to the translational motion [47]. **Figure 11** also shows that the conductivity at very low frequency (ca 10^{-2} Hz) which is corresponds to σ_{dc} , and it is much smaller than σ_{ac} . The energy required to remove one electron from one site to another within the film structure (W_m) or binding energy, can be calculated from the following relation [48]:

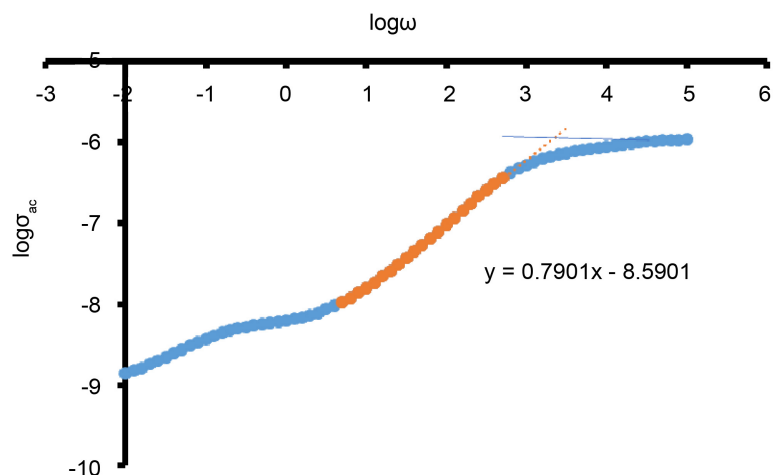


Figure 11. $\log \sigma_{ac}$ vs $\log \omega$ for $\text{TiO}_2/\text{PThA}/\text{PBTh}/\text{FTO}$ in acetate electrolyte (pH 6) at 298 K, in dark.

$$W_m = \frac{6k_B T}{1-s} \quad (12)$$

The obtained s value is corresponding to W_m of 1.233×10^{-19} J or 0.76 eV. The minimum hopping distance R_{\min} can be calculated as follow [48]:

$$R_{\min} = \frac{2e^2}{\pi \epsilon \epsilon_0 W_m} \quad (13)$$

The hopping distance R_{\min} corresponding to the calculated W_m is 15 nm. Both W_m and R_{\min} are temperature dependent, they generally decreases as temperature increases if s decreases with increasing temperature. The data plotted in **Figure 11** were closer to those reported under illumination. No change in s value was reported.

3.3. Band-Energy Map of $\text{TiO}_2/\text{PThA}/\text{PBTh}$

Mott-Schottky plot of $\text{TiO}_2/\text{PThA}/\text{PBTh}$ in acetate electrolyte was generated using 1 KHz with a sinusoidal signal of 10 mV peak to peak amplitude (**Figure 12**). The slope indicates a carrier density (holes) $N_D = 2.93 \times 10^{19}$. The intercept indicates the position of flat band potential (E_f) at 0.40V vs Ag/AgCl or at 5.4 eV on vacuum scale. In similar studies on the host film PBTh, the value for N_D was 9.67×10^{19} , with no changes in E_f values. This indicates that the only change that occlusion of TiO_2/PThA in PBTh caused was a lowering of the carrier density. Closer look at the CV's displayed in **Figures 6-8**, the current recorded upon illumination exceeds that recorded in dark at ≈ 0.4 V vs Ag/AgCl or at ≈ 0.6 V vs SHE. This potential was assumed to be E_f and it is confirmed by Mott-Schottky plot. This also indicates that E_f did not change by changing the electrolyte.

The data listed in **Table 1** were used to generate an energy map displayed in **Figure 13**. This figure illustrates the formation of a hybrid sub-band energy level that organizes the charge transfer at the $\text{TiO}_2/\text{PThA}/\text{PBTh}$. Hybridization between hole-like and electron-like sub-band states takes place in close proximity

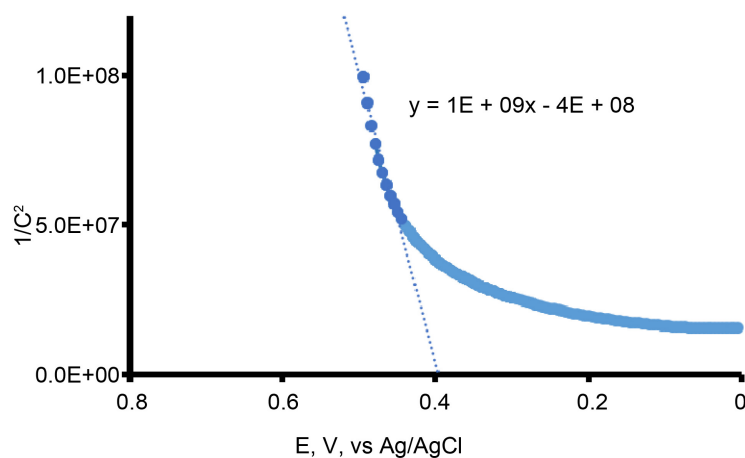


Figure 12. Mott Schottky plot of $\text{TiO}_2/\text{PThA}/\text{PBTh}$ in 0.2 M acetate electrolyte pH 6.

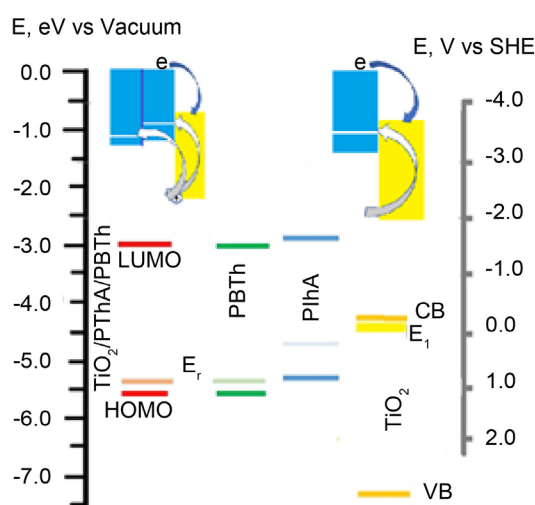


Figure 13. Energy map for $\text{TiO}_2/\text{PThA}/\text{PBTh}$ interface.

to the Fermi level. The difference between the energy level of the hybrid band and valance band (VB) represents a hole barrier height of TiO_2 being ~ 2.2 eV. That is more negative than the VB of TiO_2 . When the magnitude of the hybrid band has more negative potential (~ 2.2 V) than VB, attraction to the hole is stronger than at a less negative potential. This makes the charge transfer process via hole transfer more likely. This rule out electrons participation in the charge transfer process. This is because the electron barrier height is ~ 1.3 eV which is ~ 1.3 V more positive than the potential of the electrons in the LUMO of the modifier PThA. At the PThA/ TiO_2 , the electrons are concentrated at a lower energy level than the LUMO. This causes the electron barrier height to be even lower than the calculated value (~ 1.3 eV).

4. Conclusion

EIS studies revealed that the assembly film of $\text{TiO}_2/\text{PThA}/\text{PBTh}$ possesses a

porous-type structure. It also confirmed the approximate value of E_f obtained from electrochemical studies. Guided by the properties of the host PBTh, some optical properties such as (E_o) oscillator energy, and (E_d) dispersion energy, σ_{opt} and σ_{ele} ($\equiv \sigma_{dc}$) were calculated. EIS was used to calculate σ_{ac} and σ_{dc} . Both EIS and optical studies indicated that ac conductivity is much greater than dc conductivity. Data listed in **Table 1** indicate that no large changes in the energy band structure due to the occlusion of TiO_2 in organic films occurs. The fact that the σ_{opt} of the assembly is less than σ_{opt} of PBTh indicates that occlusion of modified TiO_2 nanoparticles into the network structure of PBTh; 1) inhibited the energy dissipation process, and 2) impeded charge polarization process of the material. Photoelectrochemical results show that the behavioral outcome of the assemblies was dominated by poly bithiophene. Possible band alignments between the organic film and TiO_2 nanoparticles, cause formation of hybrid sub-bands. Furthermore, inclusion of TiO_2 in the thiophene-based polymers enhanced the charge separation, and consequently charge transfer processes. The PBTh, PThA, and amorphous TiO_2 have band gaps that allow absorption of broad wavelengths in the blue zone which makes both materials and their I/O/O/I assemblies potentially useful in solar energy harvesting systems.

Acknowledgements

The authors acknowledge Office of the Academic Affairs, at Indiana University Kokomo for supporting this project.

Conflicts of Interest

The authors declare no conflicts of interest regarding the publication of this paper.

References

- [1] Wei, H., Yan, X., Wu, S., Luo, Z., Wei, S. and Guo, Z. (2012) Electropolymerized Polyaniline Stabilized Tungsten Oxide Nanocomposite Films: Electrochromic Behavior and Electrochemical Energy Storage. *The Journal of Physical Chemistry C*, **116**, 25052-25064. <https://doi.org/10.1021/jp3090777>
- [2] Braun, S., Osikowicz, W., Wang, Y. and Salaneck, W.R. (2007) Energy Level Alignment Regimes at Hybrid Organic-Organic and Inorganic-Organic Interfaces. *Organic Electronics*, **8**, 14-20. <https://doi.org/10.1016/j.orgel.2006.10.006>
- [3] Ananthakumar, S., Ramkumar, J. and Moorthy Babu, S. (2014) Synthesis of Thiol Modified CdSe Nanoparticles/ P_3HT Blends for Hybrid Solar Cell Structures. *Materials Science in Semiconductor Processing*, **22**, 44-49. <https://doi.org/10.1016/j.mssp.2014.02.008>
- [4] Otero, M., Dittrich, T., Rappich, J., Heredia, D.A., Fungo, F., Durantini, E. and Otero, L. (2015) Photoinduced Charge Separation in Organic-Inorganic Hybrid System: C_{60} -Containing Electropolymer/ CdSe -Quantum Dots. *Electrochimica Acta*, **173**, 316-322. <https://doi.org/10.1016/j.electacta.2015.05.029>
- [5] Zhong, Y.F., Akira, T., Geng, Y.F., Wei, Q.S., Kazuhito, H. and Keisuke, T. (2013) Donor/Acceptor Interface Modifications in Organic Solar Cells. *Journal of Photo-*

polymer Science and Technology, **26**, 181-184.

<https://doi.org/10.2494/photopolymer.26.181>

- [6] Chen, Y.F., Tamblyn, I. and Quek, S.Y. (2017) Energy Level Alignment at Hybridized Organic-Metal Interfaces: The Role of Many-Electron Effects. *The Journal of Physical Chemistry C*, **121**, 13125-13134. <https://doi.org/10.1021/acs.jpcc.7b00715>
- [7] Li, Y., et al. (2015) Enhancing Photoelectrical Performance of Dye-Sensitized Solar Cell by Doping SrTiO₃: Sm³⁺@ SiO₂ Core-Shell Nanoparticles in the Photoanode. *Electrochimica Acta*, **173**, 656-664. <https://doi.org/10.1016/j.electacta.2015.05.116>
- [8] Rather, R.A., Singh, S. and Pal, B. (2017) A C₃N₄ Surface Passivated Highly Photoactive Au-TiO₂ Tubular Nanostructure for the Efficient H₂ Production from Water under Sunlight Irradiation. *Applied Catalysis B: Environmental*, **213**, 9-17. <https://doi.org/10.1016/j.apcatb.2017.05.002>
- [9] Teoh, W.Y., Scott, J.A. and Amal, R. (2012) Progress in Heterogeneous Photocatalysis: From Classical Radical Chemistry to Engineering Nanomaterials and Solar Reactors. *The Journal of Physical Chemistry Letters*, **3**, 629-639. <https://doi.org/10.1021/jz3000646>
- [10] Lee, J.S., You, K.H. and Park, C.B. (2012) Highly Photoactive, Low Bandgap TiO₂ Nanoparticles Wrapped by Graphene. *Advanced Materials*, **24**, 1084-1088. <https://doi.org/10.1002/adma.201104110>
- [11] Karandikar, P.R., Lee, Y.-J., Kwak, G., Woo, M.H., Park, S.-J., Park, H.-G., Ha, K.-S. and Jun, K.-W. (2014) Co₃O₄@Mesoporous Silica for Fischer-Tropsch Synthesis: Core-Shell Catalysts with Multiple Core Assembly and Different Pore Diameters of Shell. *The Journal of Physical Chemistry C*, **118**, 21975-21985. <https://doi.org/10.1021/jp504936k>
- [12] Lamberti, A. (2018) ZnO- and TiO₂-Based Nanostructures. *Nanomaterials*, **8**, 325. <https://doi.org/10.3390/nano8050325>
- [13] Singh, R. and Dutta, S. (2018) Synthesis and Characterization of Solar Photoactive TiO₂ Nanoparticles with Enhanced Structural and Optical Properties. *Advanced Powder Technology*, **29**, 211-219. <https://doi.org/10.1016/j.apt.2017.11.005>
- [14] González, E., Bonnefond, A., Barrado, M., Barrasa, C., Aurora, M., Asua, J.M. and Leiza, J.R. (2015) Photoactive Self-Cleaning Polymer Coatings by TiO₂ Nanoparticle, Pickering Miniemulsion Polymerization. *The Chemical Engineering Journal*, **281**, 209-217.
- [15] Gun, Y., Song, G.Y., Quy, V.H.V., Heo, J., Lee, H., Ahn, K.-S. and Kang, S.H. (2015) Joint Effects of Photoactive TiO₂ and Fluoride-Doping on SnO₂ Inverse Opal Nanoarchitecture for Solar Water Splitting. *ACS Applied Materials & Interfaces*, **7**, 20292-20303. <https://doi.org/10.1021/acsami.5b05914>
- [16] Villatte, G., et al. (2015) Photoactive TiO₂ Antibacterial Coating on Surgical External Fixation Pins for Clinical Application. *International Journal of Nanomedicine*, **10**, 3367-3375. <https://doi.org/10.2147/IJN.S81518>
- [17] Lee, S.-W., Ahn, K.-S., Zhu, K., Neale, N.R. and Frank, A.J. (2012) Effects of TiCl₄ Treatment of Nanoporous TiO₂ Films on Morphology, Light Harvesting, and Charge-Carrier Dynamics in Dye-Sensitized Solar Cells. *The Journal of Physical Chemistry C*, **116**, 21285-21290. <https://doi.org/10.1021/jp3079887>
- [18] Tunc, I., Bruns, M., Gliemann, H., Grunze, M. and Koelsch, P. (2010) Bandgap Determination and Charge Separation in Ag@ TiO₂ Core Shell Nanoparticle Films. *Surface and Interface Analysis*, **42**, 835-841. <https://doi.org/10.1002/sia.3558>
- [19] Nuño, M., Ball, R.J., Bowen, C.R., Kurchania, R. and Sharma, G. (2015) Photocatalytic Activity of Electrophoretically Deposited (EPD) TiO₂ Coatings. *Journal of Ma-*

- terials Science*, **50**, 4822-4835. <https://doi.org/10.1007/s10853-015-9022-0>
- [20] Rahman, A., et al. (2015) Surface Modification of Natural Fiber Using Bi₂O₃/TiO₂ Composite for Photocatalytic Self-Cleaning. *BioResources*, **10**, 7405-7418. <https://doi.org/10.15376/biores.10.4.7405-7418>
- [21] Keddami, M., Senyari, S., Takenouti, H. and Bernard, P. (1994) A Composite Electrode for Studying Powdered Electroactive Materials: Preparation and Performance. *Journal of Applied Electrochemistry*, **24**, 1037-1043. <https://doi.org/10.1007/BF00241196>
- [22] Anani, A., Mao, Z., Srinivasan, S. and Appleby, A.J. (1991) Dispersion Deposition of Metal-Particle Composites and the Evaluation of Dispersion Deposited Nickel-Lanthanum Nickelate Electrocatalyst for Hydrogen Evolution. *Journal of Applied Electrochemistry*, **21**, 683-689. <https://doi.org/10.1007/BF01034046>
- [23] Hovestad, A. and Janssen, L.J.J. (1995) Electrochemical Codeposition of Inert Particles in a Metallic Matrix. *Journal of Applied Electrochemistry*, **25**, 519-527. <https://doi.org/10.1007/BF00573209>
- [24] Beck, P., Dahhaus, M. and Zahedi, N.N. (1992) Anodic Codeposition of Polypyrrole and Dispersed TiO₂. *Electrochimica Acta*, **37**, 1265-1272. [https://doi.org/10.1016/0013-4686\(92\)85066-T](https://doi.org/10.1016/0013-4686(92)85066-T)
- [25] De Tacconi, N.R., Wenren, H. and Rajeshwar, K. (1997) Photoelectrochemical Behavior of Nanocomposite Films of Cadmium Sulfide, or Titanium Dioxide, and Nickel. *Journal of the Electrochemical Society*, **144**, 3159-3163. <https://doi.org/10.1149/1.1837975>
- [26] Kasem, K., Olsen, J.C., Baker, K., Santucci, C., Lalla, J. and Willman, A.N. (2016) Electrochemical Studies on a Photoactive CdS. *Synthetic Metals*, **217**, 61-67. <https://doi.org/10.1016/j.synthmet.2016.03.013>
- [27] Kasem, K.K., Elmasry, M., Baker, K. and Santucci, C. (2017) Photoelectrochemical and Magnetic Studies on Photoactive Interface Thin Solid Film Assemblies. *Thin Solid Films*, **634**, 56-65. <https://doi.org/10.1016/j.tsf.2017.05.016>
- [28] Tauc, J. (1968) Optical Properties and Electronic Structure of Amorphous Ge and Si. *Materials Research Bulletin*, **3**, 37-46. [https://doi.org/10.1016/0025-5408\(68\)90023-8](https://doi.org/10.1016/0025-5408(68)90023-8)
- [29] Urbach, F. (1953) The Long-Wavelength Edge of Photographic Sensitivity and of the Electronic Absorption of Solids. *Physical Review*, **92**, 1324. <https://doi.org/10.1103/PhysRev.92.1324>
- [30] Wemple, S.H. and DiDomenico, M.D. (1971) Behavior of the Electronic Dielectric Constant in Covalent and Ionic Materials. *Physical Review B*, **3**, 1338-1351.
- [31] Kumar, G.A., Thomas, J., George, N., Kumar, B.A., Shnan, P.R., Npoori, V.P., Vallabhan, C.P.G. and Unnikrishnan, N.V. (2001) Optical Absorption Studies of Free (H₂Pc) and Rare Earth (RePc) Phthalocyanine Doped Borate Glasses. *Physics and Chemistry of Glasses*, **41**, 89-93.
- [32] Wu, M.T., Yao, X., Yuan, Z.H., Sun, H.T., Wu, W.C., Chen, O.H. and Xu, G.Y. (1993) Effect of Noble Metal Catalyst on Titania Exhaust Gas Oxygen Sensor. *Sensors and Actuators B*, **14**, 491. [https://doi.org/10.1016/0925-4005\(93\)85060-N](https://doi.org/10.1016/0925-4005(93)85060-N)
- [33] Dressel, M. (2002) *Electrodynamics of Solids Optical Properties of Electrons in Matter*. Cambridge University Press, Cambridge, UK.
- [34] Pankaj, S. and Katyal, S.C. (2007) Determination of Optical Parameters of alpha (As₂Se₃)₉₀Ge₁₀ Thin Film. *Journal of Physics D: Applied Physics*, **40**, 2115-2120. <https://doi.org/10.1088/0022-3727/40/7/038>

- [35] Sabari Girisum, T.C. and Dhanushkodi, S. (2009) Linear and Nonlinear Optical Properties of Tris Thiourea Zincsulphate Single Crystals. *Crystal Research and Technology*, **44**, 1297-1302. <https://doi.org/10.1002/crat.200900351>
- [36] Saranraj, A., Sahaya, S., Jude, D., Vinitha, G. and Martin Britto Dhas, S.A. (2017) Third Harmonic Generation and Thermos-Physical Properties of Benzophenone Single Crystal for Phototonic Applications. *Materials Research Express*, **4**, Article ID: 106204. <https://doi.org/10.1088/2053-1591/aa8b7b>
- [37] Drude, P. (1900) Zur Elektronentheorie der Metalle. *Annalen der Physik*, **306**, 566-613. <https://doi.org/10.1002/andp.19003060312>
- [38] Sookhakian, M., Amin, Y.M., Baradaran, S., Tajabadi, M.T., MoradiGolsheikh, A. and Basirun, W.J. (2014) A Layer-by-Layer Assembled Graphene/Zinc Sulfide/Polypyrrole Thin-Film Electrode via Electrophoretic Deposition for Solar Cells. *Thin Solid Films*, **552**, 204-211. <https://doi.org/10.1016/j.tsf.2013.12.019>
- [39] Mohammad, A., Gary, K.C.L. and Matthews, R.W. (1990) Effects of Common Inorganic Anions on Rates of Photocatalytic Oxidation of Organic Carbon over Illuminated Titanium Dioxide. *The Journal of Physical Chemistry*, **94**, 6820-6825.
- [40] Cerviño, R.M., Triaca, W.E. and Arvia, A.J. (1984) Phenomenology Related to the Kinetics of Kolbe Electrosynthesis. *Journal of Electroanalytical Chemistry*, **172**, 255-264. [https://doi.org/10.1016/0022-0728\(84\)80190-4](https://doi.org/10.1016/0022-0728(84)80190-4)
- [41] Kaiser, H., Beccu, K.D. and Gutjahr, M.A. (1976) Abschätzung der porenstruktur poröser elektroden aus impedanzmessungen. *Electrochimica Acta*, **21**, 539-543. [https://doi.org/10.1016/0013-4686\(76\)85147-X](https://doi.org/10.1016/0013-4686(76)85147-X)
- [42] Randel, J.E.B. (1947) Kinetics of Rapid Electrode Reactions. *Discussions of the Faraday Society*, **1**, 11-19. <https://doi.org/10.1039/df9470100011>
- [43] Joshi, J.H., Kanchan, D.K., Joshi, M.J., Jethva, H.G. and Parikh, K.D. (2017) Dielectric Relaxation Complex Impedance and Modulus Spectroscopy. *Materials Research Bulletin*, **93**, 61-73. <https://doi.org/10.1016/j.materresbull.2017.04.013>
- [44] Gopal Reddy, T. and Rajesh Kumar, B. (2011) Structural and Dielectric Properties of Barium Bismuth Titanate ($\text{BaBi}_4\text{Ti}_4\text{O}_{15}$) Ceramics. *International Journal of Applied Engineering Research*, **6**, 571-570.
- [45] Joshia, J.H., Kanchan, D.K., Joshi, M.J., Jethva, H.O. and Parikh, K.D. (2017) Dielectric Relaxation, Complex Impedance and Modulus Spectroscopic Studies of Mix Phase Rod Like Cobalt Sulfide Nanoparticles. *Materials Research Bulletin*, **93**, 63-73. <https://doi.org/10.1016/j.materresbull.2017.04.013>
- [46] Jonscher, A.K. (1997) The "Universal" Dielectric Response. *Nature*, **267**, 673-679. <https://doi.org/10.1038/267673a0>
- [47] Funke, K. (1993) Jump Relaxation in Solid Electrolytes. *Progress in Solid State Chemistry*, **22**, 111-195. [https://doi.org/10.1016/0079-6786\(93\)90002-9](https://doi.org/10.1016/0079-6786(93)90002-9)
- [48] Hayat, K., Rafiq, M.A., Durrani, S.K. and Hasan, M.M. (2011) Impedance Spectroscopy and Investigation of Conduction Mechanism in BaMnO_3 Nanorods. *Physica B: Condensed Matter*, **406**, 309-314. <https://doi.org/10.1016/j.physb.2010.09.026>